

# DELTA-CHB STATCOM WITH REDUCED CAPACITANCE THROUGH THIRD HARMONIC INJECTION

Dayane do Carmo Mendonça<sup>1</sup>, João Marcus Soares Callegari<sup>1</sup>, Allan Fagner Cupertino<sup>2</sup>, Heverton Augusto Pereira<sup>3</sup>, Seleme Isaac Seleme Júnior<sup>4</sup>

<sup>1</sup>Federal University of Minas Gerais, Graduate Program in Electrical Engineering, Belo Horizonte – MG, Brazil

<sup>2</sup>Federal Center for Technological Education of Minas Gerais, Department of Electrical Engineering, Belo Horizonte – MG, Brazil

<sup>3</sup>Federal University of Viçosa, Department of Electrical Engineering, Viçosa – MG, Brazil

<sup>4</sup>Federal University of Minas Gerais, Department of Electronic Engineering, Belo Horizonte – MG, Brazil

e-mail: dayane.carmo.mend@gmail.com, jmscallegari@ufmg.br, afcupertino@ieee.org, heverton.pereira@ufv.br, seleme@cpdee.ufmg.br

**Abstract** – This work investigates the third harmonic circulating current injection in delta-connected Cascaded H-Bridge (Delta-CHB) STATCOM, aiming the cell capacitance volume reduction. Firstly, analytical expressions for capacitor voltage ripple are derived without and with third harmonic injection. These expressions are used to obtain the third harmonic current waveform which minimizes the sum of capacitor voltages ripple in the whole operation range. These expressions are validated in an experimental setup based on 620 VA/220 V cell. Although this approach minimizes the ripple, an increase in the semiconductors current effort is expected. This paper quantifies the increase through analytical expressions and proposes an improved third-harmonic injection scheme which injects the third harmonic in a range of operating points. The performance of the proposed strategy is evaluated for a 17 MVA/13.8 kV Delta-CHB STATCOM with 24 cells per cluster. The results indicate a reduction of 17.2% in the theoretical cell capacitance. A physical realization of cell capacitor reveals that the proposed scheme, in the best scenario, reduces the volume in 25%. Finally, if the same power module and heatsink are employed, the proposed scheme leads to an increase in junction temperature of 13°C for IGBT and diode.

**Keywords** – Capacitor Voltage, Circulating Current, Delta-CHB, Energy Storage Requirements, STATCOM, Third Harmonic.

## I. INTRODUCTION

Delta-CHB has emerged as an interesting topology for Static Synchronous Compensator (STATCOM) applications and some manufacturers already market STATCOMs based on this converter, as illustrated in Table I.

A major disadvantage of this topology is the low-frequency ripple in the cell voltage, which leads to high energy storage requirements (approximately 10 times more than a two-level converter for the same rated power [4]). Therefore, capacitors

**TABLE I**  
Commercial STATCOMs Based Delta-CHB [1]–[3]

Product	Manufacturer
SVC Light <sup>TM</sup>	ABB
GE-STATCOM <sup>TM</sup>	GE
SVC Plus <sup>TM</sup>	Siemens

represent an important percentage of the converter costs and volume.

In Delta-CHB topology, the low-frequency ripple is integrated by a second-order harmonic component [5], [6]. Due to the inherent characteristic of this converter, the zero sequence components present in the circulating current do not flow into the grid. This fact allows the insertion of high amplitudes of zero sequence currents without increasing the harmonic distortion of the grid current [7], [8].

Some proposals in the literature discuss the third harmonic circulating current injection (THCCI) in Delta-CHB. Nieves et al. [9] use THCCI to balance the capacitor voltage during negative sequence current injection. Yu et al. [10] compute the third harmonic current needed to balance the power levels of each cluster. Oghorada and Zhang [11] use THCCI to extend the STATCOM operating ranges when used for positive and negative sequence reactive current compensation. Rodriguez et al. [12] uses an optimal THCCI to enhance the operation range of low-capacitance STATCOMs in inductive operation.

Also, other works in the literature discuss the reduction in the capacitor voltage ripple. Zhao et al. [13] presents comparative analysis of capacitor voltage ripples in Modular Multilevel Converter (MMC) with zero sequence voltage injection. The results show a reduction of 10% in the capacitor size. Li et al. [14] and Huang et al. [15] propose a modified structure of MMC and a suppressing method for capacitor voltage ripple. Townsend et al. [16], Perez and Bernet [17] propose injection of high frequency zero sequence voltage and circulating currents in MMC topology for minimize the capacitor voltage variations. Li et al. [18] presents a variation of capacitor voltage ripple according to the amplitude of injected 2nd harmonic circulating current for different operation angles of the converter.

As observed, most of the papers discuss methods to reduce the low frequency ripple in the cell voltage of MMC topology. However, Tanaka, Wang and Blaabjerg [19] investigates the

"Manuscript received 11/29/2022; first revision 02/20/2023; accepted for publication 05/22/2023, by recommendation of Editor Telles Brunelli Lazzarin. <http://dx.doi.org/10.18618/REP.2023.2.0052>"

effect of the THCCI on the capacitor ripple reduction and the electrothermal stresses on insulated gate bipolar transistor modules in Delta-CHB topology. This work explores the injection of 0 to 1 pu (capacitive operation) of third harmonic current and analyzes the power losses for these conditions. The selected third harmonic current value is the one that reduces capacitor voltage ripple and does not increase power losses when compared to the case without third harmonic injection. However, ohmic losses in the inductors were not considered (although it depends on the rms cluster current squared). Furthermore, this analysis was performed for nominal condition and only one power factor.

Finally, Mendonça et al. [20] propose the THCCI to minimize energy storage requirements of a Delta-CHB considering the entire region of operation of STATCOM. The experimental results indicate a reduction in the capacitor voltage ripple of 26.64% in capacitive operation and 62.10% in inductive operation. However, neither the real capacitor volume reduction nor the current efforts/thermal loading of the semiconductor devices are investigated in this reference. In addition, this analysis considered only the amplitude and angle that minimize the voltage ripple of the capacitors for the rated reactive power condition. Therefore, the variation of the amplitude and angle of the third harmonic is not evaluated in results of reference [20].

This paper is an extended version of [20] and discusses the injection of third harmonic current only in one range with the purpose of not increasing power losses in the entire operating range. In addition, a benchmarking between strategies that inject or not third harmonic current is performed. Current stress, dynamic performance and power losses/thermal loading are used as figures of merit. Finally, the real volume reduction is analyzed considering existing capacitors on the market. Therefore, the main goals of this work are presented:

- Comprehensive analytical modelling on the effects of the third harmonic circulating current injection in Delta-CHB STATCOM (considering the entire region of operation);
- Proposal of an injection of third harmonic current only in one range with the purpose of not increasing power losses in the entire STATCOM operating range, including a deep investigation on its real potential.

All simulation results are validated for a 17 MVA Delta-CHB STATCOM. Also, the analytical model is validated in an experimental setup based on 620 VA/220 V cell. The outline of this paper is presented as follows. Section II presents the topology and control strategy used. Section III shows the third harmonic circulating current mathematical modelling. Section IV presents the improved THCCI and Section V performs a benchmarking between strategies that inject or not third harmonic current. A capacitance realization is carried out in Section VI, with the objective of analyzing the real volume reduction of the proposed strategy. Finally, the conclusions are stated in Section VII.

## II. TOPOLOGY AND CONTROL STRATEGY

The schematic of Delta-CHB-based STATCOM is illustrated in Figure 1. The inductance  $L_{cl}$  of each cluster is responsible to reduce the high-order harmonics in the circulating current.  $C$  is the cell capacitance and  $L_f$  is the transformer inductance. The parameters of the converter are presented in Table II. This project was carried out considering a cluster reactance of 0.17 pu, a capacitor voltage ripple of 10%, and a dc-link voltage for the converter to operate in the limit between the linear region and the overmodulation. In addition, this project employs 1.7 kV IGBTs, following the guidelines proposed in [21]–[23]. The control strategy adopted is the same adopted in reference [20], which is a common control strategy for Delta-CHB converters.

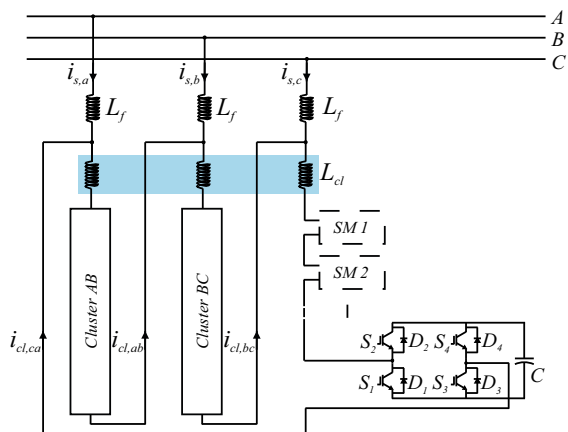


Fig. 1. Schematic of the Delta-CHB based STATCOM.

For experimental validation results, the small-scale prototype setup shown in Figure 2 is considered. The parameters are presented in Table II. In this analysis, it is considered that the converter cells are balanced and that the analytical model can be validated considering a single cell. The setup control is programmed at the Texas Instruments TMS320F28034 fixed-point digital signal processor (DSP). The dc-link voltage is controlled at the average value and a grid emulator source is connected on the cell. Moreover, the current probe A612 and differential voltage probes P5200A are used to measure the signals on Tektronix DPO 2014B oscilloscope.

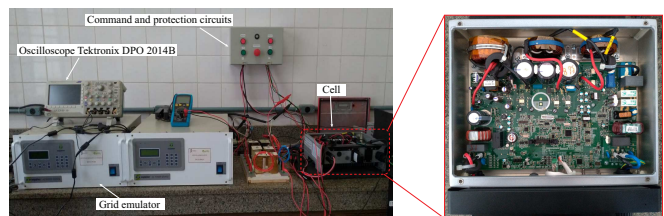


Fig. 2. Small-scale prototype setup of a single cell.

## III. THCCI MATHEMATICAL MODELLING

This section aims to develop the mathematical model for the third harmonic circulation current injection in the Delta-CHB. The capacitor and inductor ESR will not be considered in this model. The objective is to obtain the sum of the capacitor

**TABLE II**  
**Parameters of the Converter (Simulation and Experimental Setup)**

Parameter	Simulation	Experimental
Grid voltage ( $V_g$ )	13.8 kV	220 V
Effective dc-link voltage ( $V_{dc}$ )	21.58 kV	400 V
Rated power ( $S_n$ )	17 MVA	620 VA
Transformer inductance ( $L_f$ )	4.75 mH	-
Transformer X/R ratio	18	-
Cluster inductance ( $L_{cl}$ )	5 mH	2 mH
Cluster inductor X/R ratio	17	25
Cell capacitance ( $C$ )	4.172 mF	1.17 mF
Nominal cell voltage ( $v_{cell}^*$ )	899.17 V	400 V
Grid frequency ( $f_g$ )	60 Hz	60 Hz
Switching frequency ( $f_{sw}$ )	270 Hz	20 kHz
Sampling frequency ( $f_s$ )	12.96 kHz	40 kHz
Number of cells ( $N$ )	24 per cluster	-

voltages, which depends on the instantaneous power of each cluster.

The steady-state capacitor voltage can be computed based on the following assumptions:

1. The cluster instantaneous power given by  $p_{cl} = v_{cl}i_{cl}$  is delivered to the capacitor, i.e., the cell and capacitor losses were neglected;
2. The switching harmonics were neglected;
3. Voltage control follows the reference  $v_{cell}^*$ .

Under such conditions, the following expression can be obtained

$$v_{cl}i_{cl} = Nv_{cell}C\frac{dv_{cell}}{dt} \approx Nv_{cell}^*C\frac{dv_{cell}}{dt}, \quad (1)$$

where a small ripple is assumed compared to the average cell voltage.  $v_{cl}$  and  $i_{cl}$  are the cluster voltage and current of the converter,  $N$  is the number of cells,  $v_{cell}$  is the cell voltage,  $C$  is the cell capacitance and  $v_{cell}^*$  is the cell voltage reference.

The solution of (1) can be obtained through integration and defining the steady-state condition  $v_{cell} = v_{cell}^*$ . Accordingly:

$$Nv_{cell} \approx Nv_{cell}^* + \frac{1}{Cv_{cell}^*} \int v_{cl}i_{cl}dt. \quad (2)$$

The cluster current in (2) is given by:

$$i_{cl} = \frac{\hat{I}}{\sqrt{3}} \cos\left(\omega t + \theta_v + \varphi + \frac{\pi}{6}\right) + \frac{\hat{I}_{th}}{\sqrt{3}} \cos(3\omega t + 3\theta_v + \varphi_{th}), \quad (3)$$

where  $\hat{I}$  and  $\varphi$  are the amplitude and angle of the fundamental cluster current.  $\omega$  is the grid frequency in  $\frac{rad}{s}$  and  $\theta_v$  assumes the values  $(0, -\frac{2\pi}{3}, \frac{2\pi}{3})$ .  $\hat{I}_{th}$  and  $\varphi_{th}$  are the amplitude and angle of the third harmonic cluster current, given by:

$$\hat{I}_{th} = \alpha\hat{I} \text{ and } \varphi_{th} = 3\varphi + \frac{\pi}{2} + k, \quad (4)$$

where  $\alpha$  is the amplitude of the third harmonic that will be inserted according to the fundamental current and  $k$  is the phase lag between the fundamental and the third harmonic current.

The instantaneous power also depends on the cluster voltage. In addition, the injection of third harmonic current

requires a third harmonic voltage at the converter cluster voltage, as shown below:

$$v_{cl} = \sqrt{3}\hat{V} \cos\left(\omega t + \theta_v + \delta + \frac{\pi}{6}\right) + \sqrt{3}\hat{V}_{th} \cos(3\omega t + 3\theta_v + \delta_{th}), \quad (5)$$

where  $\hat{V}$  and  $\hat{V}_{th}$  are the amplitude of the fundamental and third harmonic cluster voltage.  $\delta_{th} = \varphi_{th} + \frac{\pi}{2}$ , considering the output reactance and neglecting the inductor resistance (which is a reasonable approximation in MW range). In addition,  $\hat{V}_{th} = -\frac{x_{cl,th}\hat{I}_{th}}{3}$ , where  $x_{cl,th}$  is the cluster reactance of the converter in the third harmonic frequency, i.e.,  $x_{cl,th} = 3x_{cl}$ . The  $\frac{1}{3}$  ratio refers to the internal voltage, since the circulating current is driven by the three clusters.

$\delta$  in (5) represents the angle of the fundamental cluster voltage, given by:

$$\delta = \arctan\left(\frac{x_{eq}\hat{I} \cos(\varphi)}{\hat{V}_g(1 + \Delta V_g) + x_{eq}\hat{I} \sin(\varphi)}\right), \quad (6)$$

where  $\hat{V}_g$  is the amplitude of the grid voltage and  $\Delta V_g$  is the percentual variation in the grid voltage.  $x_{eq} = \frac{x_{cl}}{3} + x_f$  is the equivalent output reactance of the STATCOM,  $x_{cl}$  is the cluster reactance and  $x_f$  is the transformer reactance.

The output voltage required for grid connected applications, when the converter injects current and assuming a negligible value of inductor resistance, is given by:

$$\hat{V} = \sqrt{\left[\hat{V}_g(1 + \Delta V_g) + x_{eq}\hat{I} \sin(\varphi)\right]^2 + \left[x_{eq}\hat{I} \cos(\varphi)\right]^2}. \quad (7)$$

Considering  $V_{dc} = Nv_{cell}^*$  and replacing the cluster current and voltage in (2), the sum of the capacitor voltage is obtained. Accordingly:

$$\begin{aligned} v_c^\Sigma = V_{dc} &+ \frac{N\hat{V}\hat{I}}{4\omega CV_{dc}} \sin\left(2\omega t + 2\theta_v + \delta + \varphi + \frac{\pi}{3}\right) \\ &+ \frac{N\hat{V}\hat{I}_{th}}{4\omega CV_{dc}} \sin\left(2\omega t + 2\theta_v - \delta + \varphi_{th} - \frac{\pi}{6}\right) \\ &+ \frac{N\hat{V}\hat{I}_{th}}{8\omega CV_{dc}} \sin\left(4\omega t + 4\theta_v + \delta + \varphi_{th} + \frac{\pi}{6}\right) \\ &+ \frac{N\hat{V}_{th}\hat{I}}{4\omega CV_{dc}} \sin\left(2\omega t + 2\theta_v + \delta_{th} - \varphi - \frac{\pi}{6}\right) \\ &+ \frac{N\hat{V}_{th}\hat{I}}{8\omega CV_{dc}} \sin\left(4\omega t + 4\theta_v + \delta_{th} + \varphi + \frac{\pi}{6}\right) \\ &+ \frac{N\hat{V}_{th}\hat{I}_{th}}{12\omega CV_{dc}} \sin\left(6\omega t + 6\theta_v + \delta_{th} + \varphi_{th}\right). \end{aligned} \quad (8)$$

Figure 3.a shows the voltage ripple of  $v_c^\Sigma$  (peak to peak) in capacitive operation ( $\varphi = \frac{\pi}{2}$ ), considering the parameters of Table II and 1 pu of fundamental current. In addition, Figure 3.b shows the voltage ripple of  $v_c^\Sigma$  (peak to peak) in inductive operation ( $\varphi = -\frac{\pi}{2}$ ).

As observed, depending on the amplitude ( $\hat{I}_{th}$ ) and angle ( $\varphi_{th}$ ) of the third harmonic current, the voltage ripple of the capacitors can be reduced. Therefore,  $\alpha$  and  $k$  which minimize the voltage ripple of the capacitors for each reactive power condition can be obtained. It is worth mentioning that the

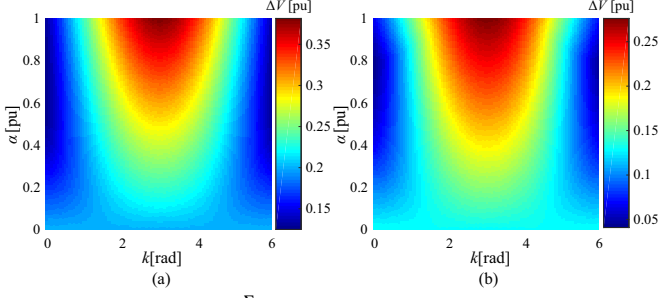


Fig. 3. Voltage ripple of  $v_c^\Sigma$  (peak to peak), considering the parameters of Table II, rated power and (a) capacitive operation; (b) inductive operation.

minimum ripple occurs when  $k = 0$ , i.e., the third harmonic is always in phase with the fundamental component.

Regarding the control strategy, the third harmonic circulating current reference is calculated according to Figure 4. The third harmonic amplitude is calculated as a function of the fundamental current component and  $\alpha$ , varying with the reactive power injected by the STATCOM. In addition, the angle of the third harmonic component is calculated as a function of the grid current in dq coordinates, the grid voltage angle ( $\theta_v$ ) and  $k$ .

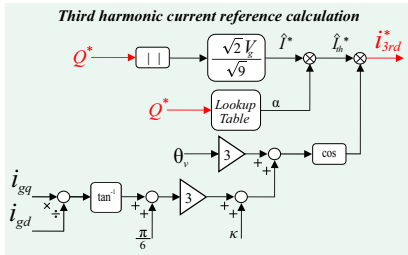


Fig. 4. Third harmonic circulating current reference computation.

Considering the experimental setup of Figure 2, the voltage ripple of  $v_c^\Sigma$  is analyzed for different conditions of  $\alpha$  and  $k$ . Figure 5.a shows the capacitor voltage ripple in capacitive operation for  $\alpha = 0$  pu and  $k=0$  rad, i.e., without third harmonic injection. Figure 5.b shows the capacitor voltage ripple for  $\alpha = 0.88$  pu and  $k = \pi$  rad, i.e., the maximum voltage ripple considering the injection of 0.88 pu of third harmonic. Moreover, the minimum capacitor voltage ripple is illustrated in Figure 5.c.

Figure 6.a shows the capacitor voltage ripple in inductive operation for  $\alpha = 0$  pu and  $k = 0$  rad, i.e., without third harmonic injection. Figure 6.b shows the capacitor voltage ripple for  $\alpha = 0.96$  pu and  $k = \pi$  rad, i.e., the maximum voltage ripple considering the injection of 0.96 pu of third harmonic. Moreover, the minimum capacitor voltage ripple is illustrated in Figure 6.c.

In addition, the cluster current and voltage are presented. As observed, the shape of the voltage ripple changes after the third harmonic injection and can be reduced depending of the amplitude and angle of the third harmonic.

In order to compare the experimental result with the analytical model, Figures 7.a and 7.b present the voltage ripple of  $v_c^\Sigma$  (peak to peak) as a function of  $\alpha$  and  $k$ , respectively. As observed, the third harmonic injection reduces the peak-to-peak voltage ripple, as expected. In addition, when the

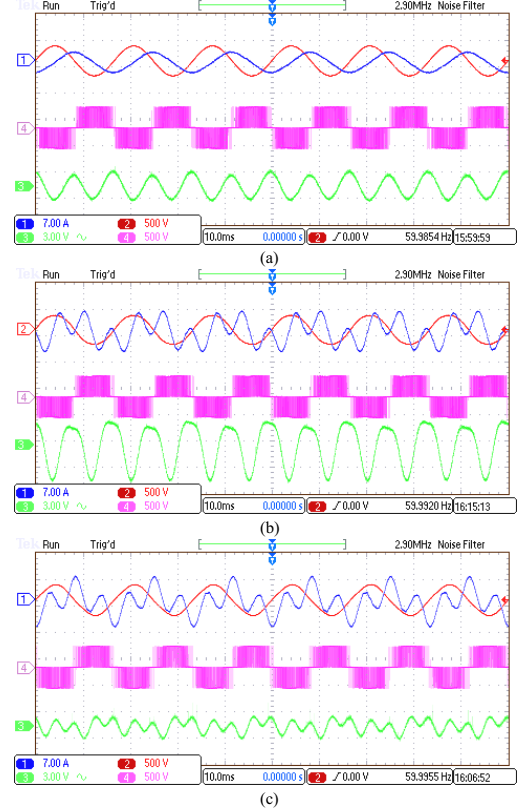


Fig. 5. Experimental results for a Delta-CHB cell 620 VA/220 V: Cluster current (Channel 1), cluster voltage (Channel 2), voltage synthesized by the converter (Channel 4) and capacitor voltage ripple (Channel 3) in capacitive operation for (a)  $\alpha = 0$  pu and  $k = 0$  rad; (b)  $\alpha = 0.88$  pu and  $k = \pi$  rad; (c)  $\alpha = 0.88$  pu and  $k = 0$  rad.

third harmonic component is not injected in phase with the fundamental current, the voltage ripple increases. Also, the analytical model can represent the experimental behavior of the voltage ripple.

#### IV. IMPROVED THCCI

Figure 8 illustrates the cell voltage in capacitive operation (higher voltage ripple). In the Strategy 1 there is no third harmonic injection and the cell voltage is in the tolerance limit of 10%. The Strategy 2 (C) shows the cell voltage for the third harmonic current which minimize the voltage ripple of the capacitors, considering the capacitance presented in Table II. As observed, the cell voltage is below the 10% tolerance limit. Thus, the capacitance value can be somehow reduced until the cell voltage reaches the tolerance limit of 10%, as illustrated for Strategy 2. In this case, a reduction of 17.2% in the capacitance value is observed. On the other hand, Strategy 1 (C reduced) considers the reduced capacitance and does not inject a third harmonic current. In this case, the cell voltage exceeds the 10% tolerance limit.

Furthermore, the capacitor voltages is not symmetrical in relation to the dc-link voltage when injecting third harmonic current, i.e.,  $\Delta V_{max}$  is different of  $\Delta V_{min}$ . However, the 10% limit on the voltage ripple of the capacitors must be considered. Basically, the upper limit is due to the voltage limit of semiconductor devices to limit losses and cosmic ray induced failures. The lower limit is defined to avoid

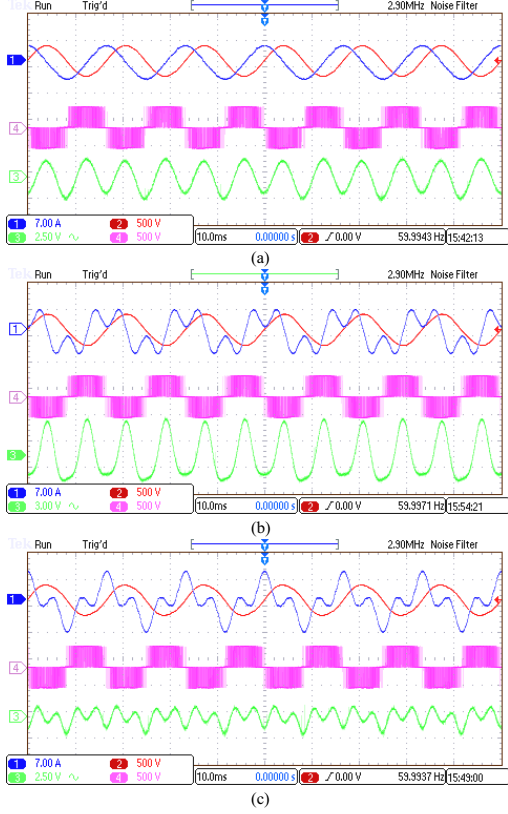


Fig. 6. Experimental results for a Delta-CHB cell of 620 VA/220 V: Cluster current (Channel 1), cluster voltage (Channel 2), voltage synthesized by the converter (Channel 4) and capacitor voltage ripple (Channel 3) in inductive operation for (a)  $\alpha = 0$  pu and  $k = 0$  rad; (b)  $\alpha = 0.96$  pu and  $k = \pi$  rad; (c)  $\alpha = 0.96$  pu and  $k = 0$  rad.

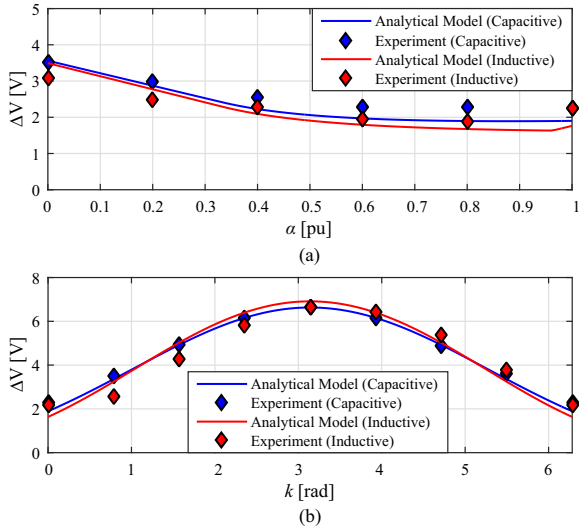


Fig. 7. Voltage ripple of  $v_c^\Sigma$  (peak to peak), considering the parameters of Table II and rated power, as a function of (a)  $\alpha$  and  $k = 0$  rad; (b)  $k$  and  $\alpha = 0.88$  pu for capacitive operation and  $\alpha = 0.96$  pu for inductive operation.

overmodulation. Therefore, the cell voltage must be limited by the maximum between  $\Delta V_{max}$  and  $\Delta V_{min}$  according the ripple factor (RF) defined below:

$$RF = \max(|\Delta V_{max}|, |\Delta V_{min}|). \quad (9)$$

The ripple factor is calculated for the Strategies presented in

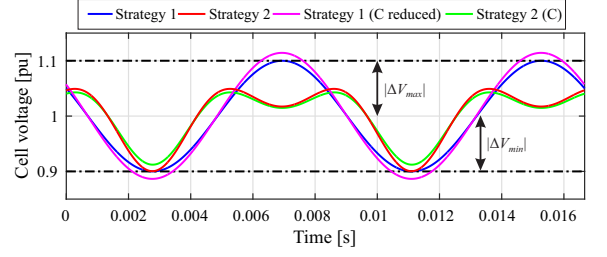


Fig. 8. Cell voltage in capacitive operation.

Figure 8 and different reactive power conditions, as illustrated in Figure 9. As observed, Strategies 1 and 2 reaches RF = 1 when  $Q = -1$ pu. However, Strategy 2 works with third harmonic injection and reduced capacitance. The THCCI across the entire reactive power operating range of the converter increases the cluster current amplitude and hence the power losses in semiconductor devices. Thus, Strategy 3 proposes injecting third harmonic current in a specific range (i.e., only when the RF of Strategy 1 (C reduced) is greater than 1).

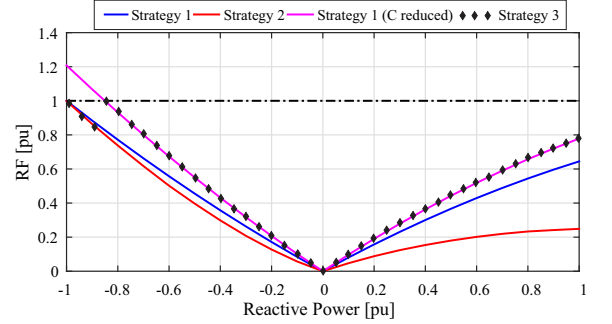


Fig. 9. Ripple factor as function of the operating reactive power.

Figure 10 illustrates the  $\hat{I}_{th}$  that minimizes the ripple as a function of the operating reactive power for Strategies 1, 2 and 3. In addition, Strategies 2 and 3 have reduced capacitance value (17.2% reduction).

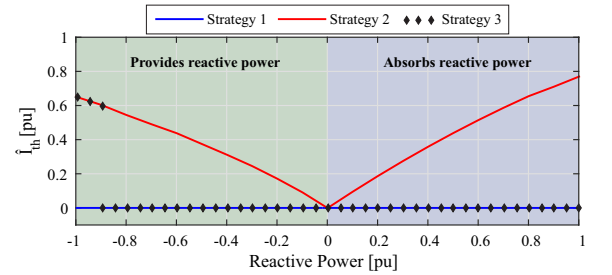


Fig. 10. Comparison of the third harmonic reference for each of the investigated techniques.

## V. BENCHMARKING

This section presents a benchmarking of Strategies 1, 2 and 3. Current stress, dynamic performance and power losses are used as figures of merit.

### A. Current stress

The average and rms currents in each semiconductor device are very useful to estimate the conduction losses of the converter. In addition, the rms value of the capacitor current

leads to a conservative estimate of the capacitor losses and its temperature rise.

Analytical expressions of the current stresses in semiconductor devices and capacitors are derived in Appendix A and are validated through simulation in the software PLECS. These expressions were obtained based on the following assumptions:

- The ripple of the capacitor voltage is not considered;
- The high-frequency content present in the currents is negligible;
- Delays and non-idealities present in the modulation process are negligible;
- The losses are evenly distributed among the converter cells.

Figure 11 presents the average current in the semiconductor devices as function of the operating reactive power for Strategies 1 and 2. As observed, the average current is little influenced by the injection of the third harmonic current.

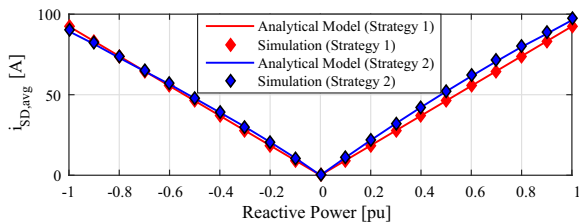


Fig. 11. Average current in the semiconductor devices (IGBT and diode) as function of the operating reactive power.

Figure 12 presents the rms current in the semiconductor devices as function of the operating reactive power for Strategies 1 and 2. As observed, Strategy 2 has a higher  $i_{SD,rms}$  value during the entire reactive power operation of the converter (37% increase compared to Strategy 1, in the worst case).

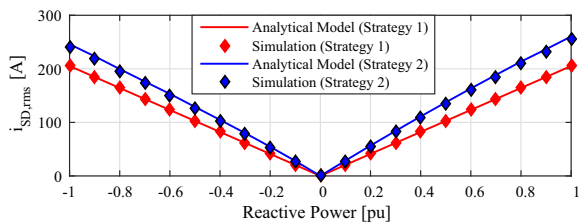


Fig. 12. rms current in the semiconductor devices (IGBT and diode) as function of the operating reactive power.

Figure 13 presents the rms current in the cell capacitor as function of the operating reactive power for Strategies 1 and 2. As observed, Strategy 2 has a lower  $i_{cap,rms}$  value during the entire reactive power operation of the converter, being more significant in inductive operation.

### B. Dynamic performance

The dynamic behavior of Strategies 1, 2 and 3 are presented in this subsection. A variation from 1 pu to -1 pu in ramp was considered in this analysis. Figure 14 illustrate the instantaneous active and reactive power for Strategies 1, 2 and 3, respectively. As can be seen, both strategies are able to supply/absorb energy from the grid. Regarding the reactive

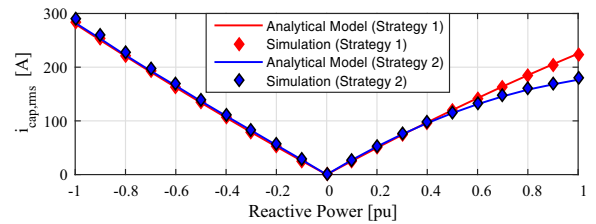


Fig. 13. rms current in the capacitor as function of the operating reactive power.

power (Figure 14.a), a very similar behavior is observed. The increase in ripple is due to harmonics in the output current. For active power (Figure 14.b), small differences are observed due to the extra losses caused by third harmonic injection. It is noteworthy that in the inductive region, strategies 1 and 3 present the same dynamics and in the capacitive region, strategies 2 and 3 present the same dynamics (at steady state).

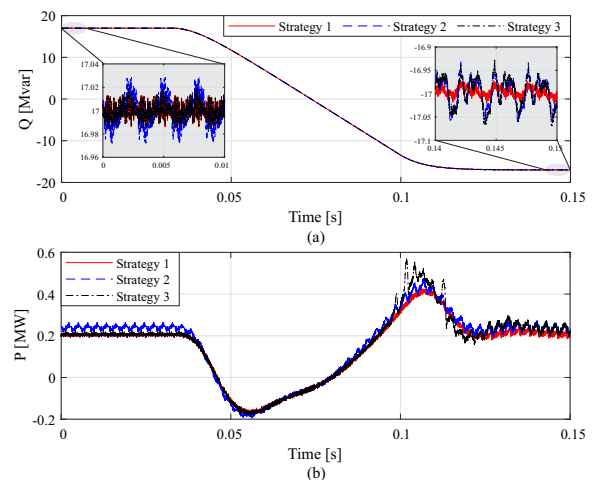


Fig. 14. Dynamic behavior of instantaneous: (a) reactive and (b) active power.

Figures 15.a, 15.b and 15.c show the output current of the converter for Strategies 1, 2 and 3, respectively. As observed, the third harmonic injection (Strategies 2 and 3) affects the current total harmonic distortion (THD). Although zero sequence control is theoretically decoupled from output current control, in practice these subsystems are coupled through the capacitor voltage ripple and modulation index. By comparing the current THD for strategies 1 and 3, before 0.03 seconds the slight THD increase is related to the capacitance reduction. On the other hand, after 0.12 seconds, the effect of the third harmonic injection is superposed. Although the THD increase is significant, its absolute value is very small due to the high number of levels. Therefore, this drawback should not be an issue for medium voltage STATCOMs.

Figures 16.a, 16.b and 16.c present the cluster current for Strategies 1, 2 and 3, respectively. This result shows the injection of the third harmonic in the whole range in Strategy 2 and the injection in only one band in Strategy 3. Furthermore, the peak of the cluster current increases with the injection of the third harmonic, because  $k = 0$  is employed.

Figures 17.a, 17.b and 17.c show the cell voltages for Strategies 1, 2 and 3, respectively. When there is no third harmonic injection (Strategy 1), the capacitor voltage ripple (average voltages) is within the 10% limit. However, the

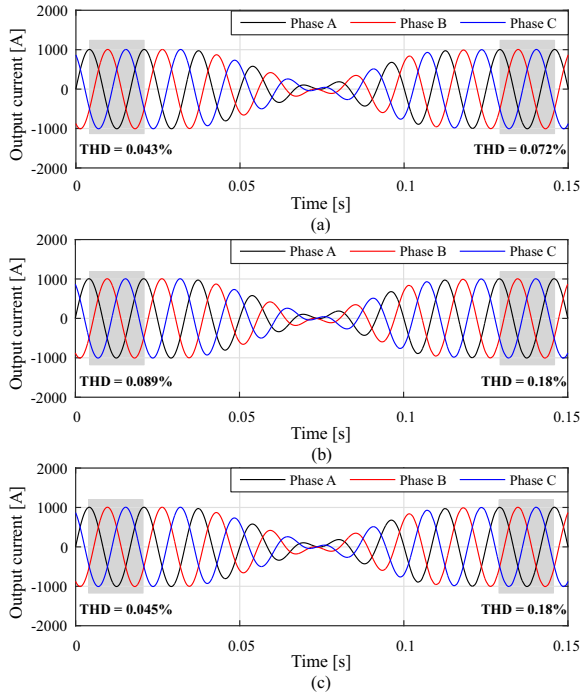


Fig. 15. Dynamic behavior of output current: (a) Strategy 1 ; (b) Strategy 2; (c) Strategy 3.

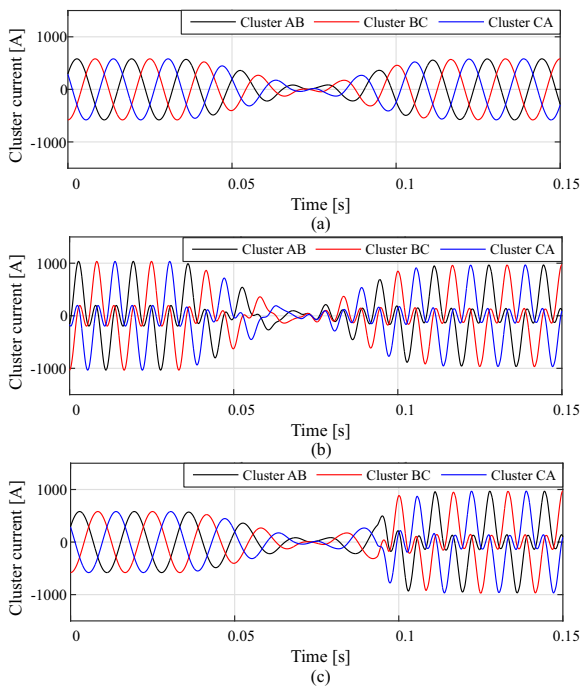


Fig. 16. Dynamic behavior of cluster current: (a) Strategy 1 ; (b) Strategy 2; (c) Strategy 3.

injection of a third harmonic across the entire reactive power range (Strategy 2) allows reducing the voltage ripple of the capacitors and consequently reducing the value of capacitance required to meet the 10% limit. Another factor to be considered is that in inductive operation, the voltage ripple of the capacitors is smaller and therefore it is not necessary to inject a third harmonic in this range, as performed in Strategy 3. Therefore, in both strategies the limit of 10% is respected.

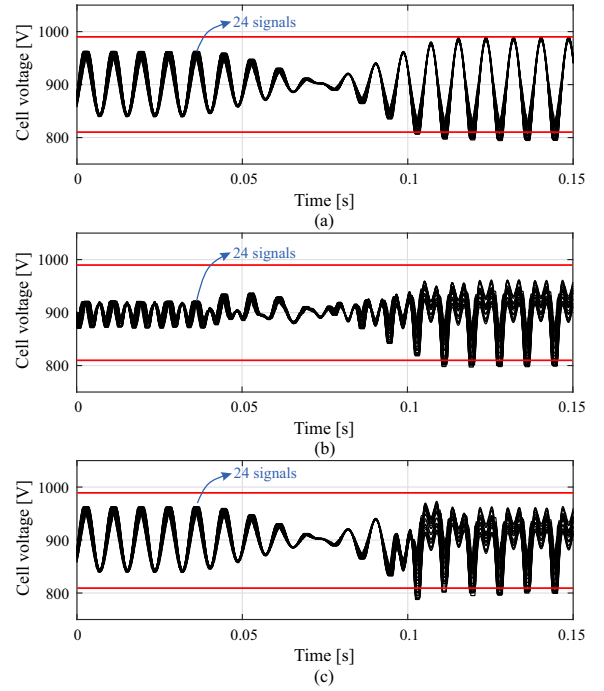


Fig. 17. Dynamic behavior of cell voltage: (a) Strategy 1 ; (b) Strategy 2; (c) Strategy 3.

### C. Power losses

The power losses for Strategies 1, 2 and 3 are calculated based on semiconductor losses and cluster inductor ohmic losses. An ABB module (IGBT + Diode) part number 5SND 0800M170100 of 1.7kV - 800A was chosen for this application. The power losses estimation is based on look-up tables using data from datasheet. Conduction losses, turn-on and turn-off energy for the IGBTs and the conduction and the reverse recovery energy for the diodes of each cell are considered [24]. Assuming that all the cell and cluster parameters are identical, the losses and thermal behavior of all cells in the clusters are similar. Hence, the loss evaluation can be simplified considering only one cluster of the converter.

Additionally, an important feature is the power losses dependence of the temperature. This information is obtained from the datasheet for the temperatures of 25 °C, 125 °C and 150 °C. Linear interpolation and extrapolation are used. In addition, the switching energies are assumed to be proportional to the blocking voltage. The hybrid electro-thermal model with the combination of Cauer and Foster model, proposed in [25], is employed for junction and case temperatures estimation. The junction-to-case and case-to-heatsink thermal impedance values were obtained in the power module datasheet.

In general, the heatsink and the cooling systems are designed to ensure steady-state junction temperatures within a safety limit (e.g., below 150 °C). The manufacturer indicates maximum values of 150 °C of junction temperature and 125 °C for case temperature. The heatsink thermal resistance was set to 0.054 K/W. This value guarantees that, in the worst case and control strategy 1, the junction temperature is 110 °C.

As observed in Figure 18, Strategy 2 presents higher power losses due to third harmonic injection in the entire reactive power range. Strategy 3 has losses equal to Strategy 2 only in

a narrow range. Otherwise, the losses are equal to Strategy 1. Despite the 37% increase in rms current (worst case) with third harmonic injection, the largest increase in conduction losses was 28%. Furthermore, the largest increase in inductor ohmic losses was 88%.

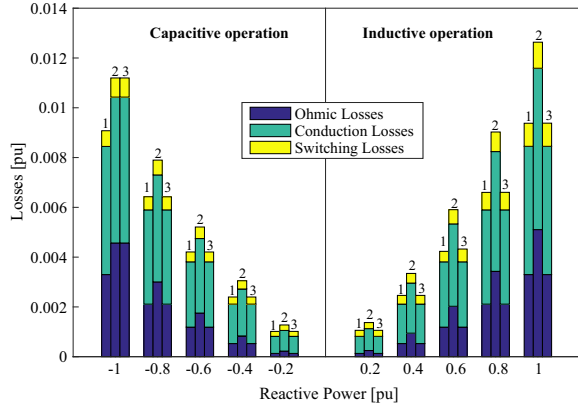


Fig. 18. Power losses with reactive power compensation variation. 1 refers to Strategy 1, 2 refers to Strategy 2 and 3 refers to Strategy 3.

Table III presents the average temperature of the semiconductor devices for the three strategies. It is possible to notice that the temperature increases with the third harmonic injection. This temperature could be reduced by improving the heat transfer mechanism (heatsink design or cooling) or by increasing the silicon area of the semiconductor devices. This analysis is not investigated here, but can be approached in future publications.

**TABLE III**  
Temperature of Semiconductor Devices

Strategy	IGBT Temperature		Diode Temperature	
	-1 pu	1 pu	-1 pu	1 pu
Strategy 1	103°C	107°C	105°C	110°C
Strategy 2	116°C	128°C	118°C	130°C
Strategy 3	116°C	107°C	118°C	110°C

## VI. CAPACITANCE REALIZATION

This section evaluates the real volume reduction considering capacitor physical realization. In this analysis, the 1100 V capacitors of the PK16 (E50) series from Electronicon were considered [26]. Table IV shows 23 part numbers evaluated, their maximum rms current and physical dimensions. The number of capacitors in parallel ( $N_C$ ) required for each cell depends on the theoretical capacitance value and the maximum rms current that the capacitors must withstand. Accordingly:

$$N_C = \text{ceil} \left( \max \left( \frac{C}{C_x}, \frac{i_{C,max}}{i_{C_x,max}} \right) \right), \quad (10)$$

where  $C$  is the theoretical capacitance value and  $C_x$  is the capacitance value for a given part number.  $i_{C,max}$  represents the maximum rms current value of the capacitor (obtained from Figure 13), considering all operating points and  $i_{C_x,max}$  represents the maximum rms current for a given part number. The function ceil is employed since the number of capacitors should be integer.

**TABLE IV**  
Parameters for Capacitance Realization

Capacitor	Capacitance (mF)	Maximum rms current (A)	Dimensions: DxL (mm)
C <sub>1</sub>	0.172	35	85 x 78
C <sub>2</sub>	0.2	30	67 x 114
C <sub>3</sub>	0.25	70	85 x 100
C <sub>4</sub>	0.28	40	85 x 95
C <sub>5</sub>	0.375	90	85 x 146
C <sub>6</sub>	0.38	40	85 x 120
C <sub>7</sub>	0.42	40	85 x 130
C <sub>8</sub>	0.45	80	85 x 150
C <sub>9</sub>	0.45	80	116 x 110
C <sub>10</sub>	0.58	80	100 x 155
C <sub>11</sub>	0.595	40	85 x 181
C <sub>12</sub>	0.65	60	85 x 210
C <sub>13</sub>	0.8	80	116 x 145
C <sub>14</sub>	0.83	60	85 x 252
C <sub>15</sub>	0.99	80	100 x 230
C <sub>16</sub>	1.1	65	116 x 180
C <sub>17</sub>	1.245	120	116 x 220
C <sub>18</sub>	1.66	120	116 x 290
C <sub>19</sub>	1.75	95	116 x 280
C <sub>20</sub>	1.85	120	136 x 220
C <sub>21</sub>	2.2	90	116 x 340
C <sub>22</sub>	2.5	60	136 x 280
C <sub>23</sub>	3.1	120	136 x 335

Figure 19 presents the number of capacitors required to meet the requirements of (10). For some part numbers there is no reduction in the number of capacitors. This is related to two causes: 1) rounding; 2) rms current requirement.

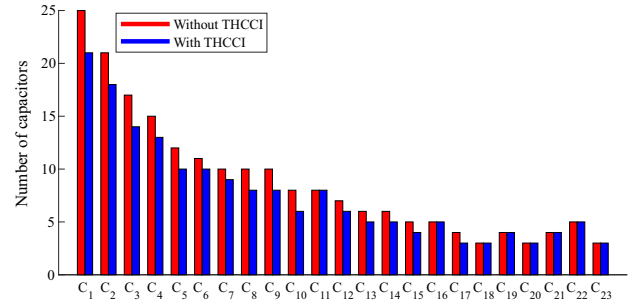


Fig. 19. Number of capacitors per cell computed through (10) and data from Table IV.

Indeed, the obtained capacitance can be higher than the theoretical capacitance value. This error was computed in Figure 20, where the highest errors are related to the part number with the highest capacitance value (C<sub>18</sub>-C<sub>23</sub>).

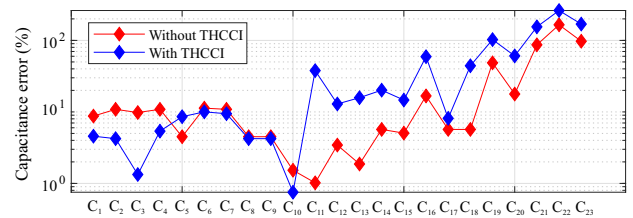


Fig. 20. Capacitance error with respect to the theoretical value. Remark: The y-axis is in logarithm.

Finally, Figure 21 shows the volume reduction provided by the proposed technique. The area between the two curves represents the volume reduction when considering the same

part number for both cases (with and without third harmonic injection). In this case, the maximum volume reduction is 25% for capacitor  $C_{10}$ . It is worth noting that different part numbers could be used in the two strategies, resulting in different volume reduction indexes.

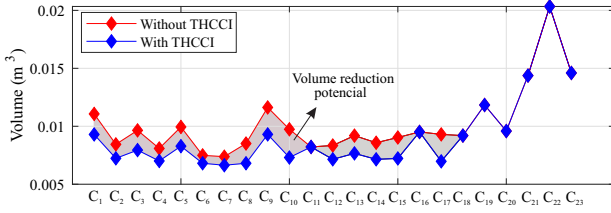


Fig. 21. Capacitor bank volume per cell.

Therefore, the real capacitance reduction is considerably affected by the selected part number. It could be as high as 25% or zero, depending on the selected part number.

## VII. CONCLUSIONS

This paper presents a mathematical modeling of third harmonic component injection in the circulating current of Delta-CHB-based STATCOM. Analytical expressions for the sum of the capacitor voltages were derived as a function of the third harmonic circulating current and evaluated in simulation and experimental results. An improved third harmonic circulating current injection is presented and a benchmarking between strategies that inject or not third harmonic current is performed.

In addition, a 17.2% reduction in the theoretical cell capacitance was observed. However, this reduction can be greater or lesser depending on the capacitance realization. A physical realization of cell capacitor reveals that the proposed scheme, in the best scenario, reduces the volume in 25%. Furthermore, if the same power module and heatsink are employed, the proposed scheme leads to an increase in junction temperature of 13 °C for IGBT and diode. This temperature could be reduced by improving the heat transfer mechanism or by increasing the silicon area of the semiconductor devices. Finally, the power losses increase when there is injection of third harmonic current (increase of 24% to -1 pu). However, the third harmonic injection of Strategy 3 only occurs between -0.85 and -1 pu. Therefore, these results indicate a cost and volume reduction in the converter.

## ACKNOWLEDGEMENTS

The authors would like to thank the National Council for Scientific and Technological Development - CNPq (Grant 408058/2021-8), and FAPEMIG (Grant APQ-02556-21) by funding. In addition, this work was carried out with the support of the CAPES (Coordenação de Aperfeiçoamento de Pessoal de Nível Superior) - Financing Code 001 and Academic Excellence Program (PROEX).

## CURRENT STRESS CALCULATION

The computation of current stresses is based on the cluster current and the cell duty-cycle. In this analysis, only the

variation in the amplitude of the third harmonic is considered, that is, the phase of the third harmonic is kept equal to zero.

Considering a positive cluster current, the devices  $S_2$ ,  $D_1$ ,  $S_4$  and  $D_3$  are capable of conducting, and the average and rms currents are given by:

$$i_{SD,avg} = \frac{1}{2\pi} \int_{\theta_X}^{\theta_Y} \lambda i_{cl} d\omega t, \quad (11)$$

$$i_{SD,rms} = \sqrt{\frac{1}{2\pi} \int_{\theta_X}^{\theta_Y} \lambda i_{cl}^2 d\omega t}, \quad (12)$$

where  $\lambda = \lambda_1$  for  $S_2$ ,  $\lambda = 1 - \lambda_1$  for  $D_1$ ,  $\lambda = \lambda_2$  for  $S_4$  and  $\lambda = 1 - \lambda_2$  for  $D_3$ .  $\theta_X$  and  $\theta_Y$  are angles that define the zero crossing of the cluster current.

Considering a negative cluster current, the devices  $S_1$ ,  $D_2$ ,  $S_3$  and  $D_4$  are capable of conducting, and the average and rms currents are given by:

$$i_{SD,avg} = \frac{1}{2\pi} \int_{\theta_X}^{\theta_Y} -\lambda i_{cl} d\omega t, \quad (13)$$

$$i_{SD,rms} = \sqrt{\frac{1}{2\pi} \int_{\theta_X}^{\theta_Y} -\lambda i_{cl}^2 d\omega t}, \quad (14)$$

where  $\lambda = 1 - \lambda_1$  for  $S_1$ ,  $\lambda = \lambda_1$  for  $D_2$ ,  $\lambda = 1 - \lambda_2$  for  $S_3$  and  $\lambda = \lambda_2$  for  $D_4$ .

The parameters  $\lambda_1$ ,  $\lambda_2$ ,  $i_{cl}$ ,  $\theta_X$  and  $\theta_Y$  are given in Table V. Figures 22.a and 22.b illustrate the cluster current for  $\alpha \leq \frac{1}{3}$  and  $\alpha > \frac{1}{3}$ , respectively. As observed, when  $\alpha > \frac{1}{3}$ , the zero crossing happens six times in half period of the cluster current (in this case, considering only the positive semi-cycle).

**TABLE V**  
**Parameters for Calculating Current Stress in Semiconductor Devices**

$\lambda_1$	$\frac{1}{2} + \frac{\sqrt{3}V}{2V_{dc}} \cos(\omega t + \frac{\pi}{6}) - \frac{\sqrt{3}i_{cl,th}\alpha t}{6V_{dc}} \cos(3\omega t + \pi + 3\varphi)$
$\lambda_2$	$\frac{1}{2} + \frac{\sqrt{3}V}{2V_{dc}} \cos(\omega t + \frac{\pi}{6} + \pi) - \frac{\sqrt{3}i_{cl,th}\alpha t}{6V_{dc}} \cos(3\omega t + 2\pi + 3\varphi)$
$i_{cl}$	$\frac{\hat{i}}{\sqrt{3}} \cos(\omega t + \varphi + \frac{\pi}{6}) + \frac{\hat{i}_h}{\sqrt{3}} \cos(3\omega t + \varphi_h)$
$\theta_1$	$\frac{4\pi}{3} - \varphi$ (for $\alpha \leq \frac{1}{3}$ ); $\cos^{-1}\left(\sqrt{\frac{3\alpha-1}{4\alpha}}\right) + \frac{5\pi}{6} - \varphi$ (for $\alpha > \frac{1}{3}$ )
$\theta_2$	$\frac{7\pi}{3} - \varphi$ (for $\alpha \leq \frac{1}{3}$ ); $\frac{4\pi}{3} - \varphi$ (for $\alpha > \frac{1}{3}$ )
$\theta_3$	$\cos^{-1}\left(-\sqrt{\frac{3\alpha-1}{4\alpha}}\right) + \frac{5\pi}{6} - \varphi$ (for $\alpha > \frac{1}{3}$ )
$\theta_4$	$\cos^{-1}\left(\sqrt{\frac{3\alpha-1}{4\alpha}}\right) + \frac{11\pi}{6} - \varphi$ (for $\alpha > \frac{1}{3}$ )
$\theta_5$	$\frac{7\pi}{3} - \varphi$ (for $\alpha > \frac{1}{3}$ )
$\theta_6$	$\cos^{-1}\left(-\sqrt{\frac{3\alpha-1}{4\alpha}}\right) + \frac{11\pi}{6} - \varphi$ (for $\alpha > \frac{1}{3}$ )

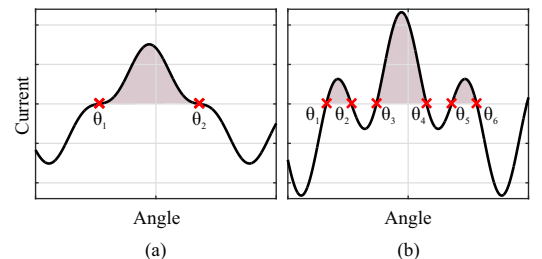


Fig. 22. Angles that define the zero crossing of the cluster current of (a)  $\alpha \leq \frac{1}{3}$ ; (b)  $\alpha > \frac{1}{3}$ .

Solving (11)–(14) for the parameters in Table V the average and rms currents are obtained. For STATCOM application, the average and rms current is the same for the eight semiconductor devices. Accordingly:

$$i_{SD,avg} = \begin{cases} f_1(\theta_1, \theta_2), & \text{if } \varphi = -\frac{\pi}{2} \text{ and } \alpha \leq \frac{1}{3}, \\ f_2(\theta_1, \theta_2), & \text{if } \varphi = \frac{\pi}{2} \text{ and } \alpha \leq \frac{1}{3}, \\ f_1(\theta_1, \theta_2) + f_1(\theta_3, \theta_4) + f_1(\theta_5, \theta_6), & \text{if } \varphi = -\frac{\pi}{2} \text{ and } \alpha > \frac{1}{3}, \\ f_2(\theta_1, \theta_2) + f_2(\theta_3, \theta_4) + f_2(\theta_5, \theta_6), & \text{if } \varphi = \frac{\pi}{2} \text{ and } \alpha > \frac{1}{3}, \end{cases} \quad (15)$$

where  $f_1(\theta_X, \theta_Y) = a + b + c$ ,  $f_2(\theta_X, \theta_Y) = -a - b + c$ , and:

$$a = -\frac{\alpha \widehat{V}(\cos(4\theta_Y) - \cos(4\theta_X))}{32V_{dc}} - \frac{3\alpha \widehat{V}(\sin(4\theta_Y) - \sin(4\theta_X))}{32\sqrt{3}V_{dc}} + \frac{(\alpha - 1)\widehat{V}(\cos(2\theta_Y) - \cos(2\theta_X))}{16V_{dc}} - \frac{3(\alpha - 1)\widehat{V}(\sin(2\theta_Y) - \sin(2\theta_X))}{16\sqrt{3}V_{dc}}, \quad (16)$$

$$b = -\frac{\alpha V_{dc}\widehat{I}(\sin(3\theta_Y) - \sin(3\theta_X))}{6\sqrt{3}V_{dc}} + \frac{V_{dc}\widehat{I}(\sin(\theta_Y) - \sin(\theta_X))}{4\sqrt{3}V_{dc}} - \frac{V_{dc}\widehat{I}(\cos(\theta_Y) - \cos(\theta_X))}{4V_{dc}}, \quad (17)$$

$$c = -\frac{\alpha^2 x_{cl,th} \widehat{I}^2 (1 + (\cos(6\theta_Y) - \cos(6\theta_X)))}{72V_{dc}} + \frac{\alpha x_{cl,th} \widehat{I}^2 (\sin(4\theta_Y + \frac{\pi}{6}) - \sin(4\theta_X + \frac{\pi}{6}))}{48V_{dc}} + \frac{\alpha x_{cl,th} \widehat{I}^2 (\cos(2\theta_Y + \frac{\pi}{3}) - \cos(2\theta_X + \frac{\pi}{3}))}{24V_{dc}}, \quad (18)$$

and

$$i_{SD,rms} = \begin{cases} f_3(\theta_1, \theta_2), & \text{if } \varphi = -\frac{\pi}{2} \text{ and } \alpha \leq \frac{1}{3}, \\ f_4(\theta_1, \theta_2), & \text{if } \varphi = \frac{\pi}{2} \text{ and } \alpha \leq \frac{1}{3}, \\ f_3(\theta_1, \theta_2) + f_3(\theta_3, \theta_4) + f_3(\theta_5, \theta_6), & \text{if } \varphi = -\frac{\pi}{2} \text{ and } \alpha > \frac{1}{3}, \\ f_4(\theta_1, \theta_2) + f_4(\theta_3, \theta_4) + f_4(\theta_5, \theta_6), & \text{if } \varphi = \frac{\pi}{2} \text{ and } \alpha > \frac{1}{3}, \end{cases} \quad (19)$$

where  $f_3(\theta_X, \theta_Y) = d + e + f + g + h$ ,  $f_4(\theta_X, \theta_Y) = d + e - f - g - h$ , and:

$$d = \frac{\widehat{V} \alpha^2 (\sin(7\theta_Y) - \sin(7\theta_X))}{112V_{dc}} + \frac{\sqrt{3}\widehat{V} \alpha (\cos(4\theta_Y) - \cos(4\theta_X))}{48} + \frac{\widehat{V} \widehat{V} (\alpha^2 - 2\alpha) (\sin(5\theta_Y) - \sin(5\theta_X))}{80V_{dc}} + \frac{\widehat{V}^2 (\alpha^2 + 1) (\theta_Y - \theta_X)}{12} - \frac{\sqrt{3}\widehat{V} \widehat{V} (\alpha^2 - 2\alpha) (\cos(5\theta_Y) - \cos(5\theta_X))}{240V_{dc}} + \frac{\widehat{V}^2 (2\alpha^2 - 2\alpha + 1) (\sin(\theta_Y) - \sin(\theta_X))}{16V_{dc}}, \quad (20)$$

$$e = \frac{\sqrt{3}\widehat{V} \alpha^2 (\cos(7\theta_Y) - \cos(7\theta_X))}{336V_{dc}} - \frac{\widehat{V}^2 \alpha (\sin(4\theta_Y) - \sin(4\theta_X))}{48} - \frac{\sqrt{3}\widehat{V} \widehat{V} (\cos(3\theta_Y) - \cos(3\theta_X))}{72V_{dc}} - \frac{\widehat{V}^2 (2\alpha + 1) (\sin(2\theta_Y) - \sin(2\theta_X))}{48} + \frac{\widehat{V}^2 \alpha^2 (\sin(6\theta_Y) - \sin(6\theta_X))}{72} - \frac{\sqrt{3}\widehat{V}^2 (2\alpha + 1) (\cos(2\theta_Y) - \cos(2\theta_X))}{48} + \frac{\sqrt{3}\widehat{V}^2 \widehat{V}_1 (2\alpha^2 - 2\alpha + 1) (\cos(\theta_Y) - \cos(\theta_X))}{48V_{dc}}, \quad (21)$$

$$f = \frac{\widehat{V}^3 x_{cl,th} \alpha (\sin(-5\theta_Y + \frac{\pi}{6}) - \sin(-5\theta_X + \frac{\pi}{6}))}{120\sqrt{3}V_{dc}} + \frac{\widehat{V} x_{eq,th} \alpha (\sin(\theta_Y) - \sin(\theta_X))}{48V_{dc}} + \frac{\widehat{V}^3 x_{cl,th} \alpha (\cos(\theta_Y) - \cos(\theta_X))}{48\sqrt{3}V_{dc}} - \frac{\widehat{V}^3 x_{cl,th} \alpha (\cos(3\theta_Y) - \cos(3\theta_X))}{36\sqrt{3}V_{dc}}, \quad (22)$$

$$g = \frac{\widehat{V}^3 x_{cl,th} \alpha^2 (\sin(-5\theta_Y + \frac{\pi}{6}) - \sin(-5\theta_X + \frac{\pi}{6}))}{60\sqrt{3}V_{dc}} + \frac{\widehat{V}^3 x_{cl,th} \alpha^2 (\sin(7\theta_Y + \frac{\pi}{6}) - \sin(7\theta_X + \frac{\pi}{6}))}{84\sqrt{3}V_{dc}}, \quad (23)$$

$$h = -\frac{\widehat{V}^3 x_{cl,th} \alpha^3 (\cos^3(3\theta_Y) - \cos^3(3\theta_X))}{54\sqrt{3}V_{dc}}. \quad (24)$$

The rms capacitor current can be calculated through the modulation signals of each arm of the full-bridge cell ( $v_{ref1}$  and  $v_{ref2}$ ) and the cluster current, as follows:

$$i_{cap,rms} = \sqrt{\frac{1}{\pi} \int_{\theta_7}^{\theta_8} \frac{v_{ref1} - v_{ref2}}{2} i_{cl}^2 d\omega t}, \quad (25)$$

where  $\theta_7$  and  $\theta_8$  represent the period in which  $v_{ref1} \geq v_{ref2}$ . These parameters are defined in Table VI.

**TABLE VI**  
Parameters for Calculating Current Stress in Cell Capacitor

$v_{ref1}$	$\frac{\sqrt{3}\widehat{V}}{V_{dc}} \cos(\omega t + \frac{\pi}{6}) - \frac{\sqrt{3}x_{cl,th}\alpha\widehat{I}}{3V_{dc}} \cos(3\omega t + \pi + 3\varphi)$
$v_{ref2}$	$\frac{\sqrt{3}\widehat{V}}{V_{dc}} \cos(\omega t + \frac{\pi}{6} + \pi) - \frac{\sqrt{3}x_{cl,th}\alpha\widehat{I}}{3V_{dc}} \cos(3\omega t + 2\pi + 3\varphi)$
$\theta_7$	$\frac{4\pi}{3}$
$\theta_8$	$\frac{7\pi}{3}$

Solving (25) for the parameters in Table VI the rms capacitor current is obtained. Accordingly:

$$i_{cap,rms} = \begin{cases} i + j + l + m + n, & \text{if } \varphi = -\frac{\pi}{2}, \\ i - j - l + m - n, & \text{if } \varphi = \frac{\pi}{2}, \end{cases} \quad (26)$$

where  $i$ ,  $j$ ,  $l$ ,  $m$  and  $n$  are given by:

$$i = -\frac{\widehat{V}^2 \widehat{V} (\sin^3(\theta_Y + \frac{\pi}{6}) - \sin^3(\theta_X + \frac{\pi}{6}))}{3\sqrt{3}V_{dc}} + \frac{\widehat{V}^2 \widehat{V} \alpha (\sin(-5\theta_Y + \frac{\pi}{6}) - \sin(-5\theta_X + \frac{\pi}{6}))}{10\sqrt{3}V_{dc}} - \frac{\widehat{V}^2 \widehat{V} \alpha (\sin(\theta_Y) - \sin(\theta_X))}{4V_{dc}} - \frac{\widehat{V}^2 \widehat{V} \alpha (\cos(\theta_Y) - \cos(\theta_X))}{4\sqrt{3}V_{dc}}, \quad (27)$$

$$j = -\frac{\widehat{V}^2 \widehat{V} \alpha^2 (\sin(-5\theta_Y + \frac{\pi}{6}) - \sin(-5\theta_X + \frac{\pi}{6}))}{20\sqrt{3}V_{dc}} + \frac{\widehat{V}^2 \widehat{V} \alpha^2 (\sin(7\theta_Y + \frac{\pi}{6}) - \sin(7\theta_X + \frac{\pi}{6}))}{28\sqrt{3}V_{dc}} + \frac{\widehat{V}^2 \widehat{V} \alpha^2 (\sin(\theta_Y) - \sin(\theta_X))}{4V_{dc}} + \frac{\widehat{V}^2 \widehat{V} \alpha^2 (\cos(\theta_Y) - \cos(\theta_X))}{4\sqrt{3}V_{dc}}, \quad (28)$$

$$l = \frac{\widehat{V}^3 x_{cl,th} \alpha (\sin(-5\theta_Y + \frac{\pi}{6}) - \sin(-5\theta_X + \frac{\pi}{6}))}{60\sqrt{3}V_{dc}} + \frac{\widehat{V}^3 x_{cl,th} \alpha (\sin(\theta_Y) - \sin(\theta_X))}{24V_{dc}} + \frac{\widehat{V}^3 x_{cl,th} \alpha (\cos(\theta_Y) - \cos(\theta_X))}{24\sqrt{3}V_{dc}} - \frac{\widehat{V}^3 x_{cl,th} \alpha (\cos(3\theta_Y) - \cos(3\theta_X))}{18\sqrt{3}V_{dc}}, \quad (29)$$

$$m = \frac{\widehat{V}^3 x_{cl,th} \alpha^2 (\sin(-5\theta_Y + \frac{\pi}{6}) - \sin(-5\theta_X + \frac{\pi}{6}))}{30\sqrt{3}V_{dc}} + \frac{\widehat{V}^3 x_{cl,th} \alpha^2 (\sin(7\theta_Y + \frac{\pi}{6}) - \sin(7\theta_X + \frac{\pi}{6}))}{30\sqrt{3}V_{dc}}, \quad (30)$$

$$n = -\frac{\hat{P}_{x_{cl,th}}\alpha^3(\cos^3(3\theta_y) - \cos^3(3\theta_x))}{27\sqrt{3}V_{dc}}. \quad (31)$$

## REFERENCES

- [1] ABB, *Static compensator (STATCOM)*, 2019, URL: <https://new.abb.com/facts/statcom>, accessed: 16-Sep-2019.
- [2] GE, *Static Synchronous Compensator (STATCOM) Solutions*, 2019, URL: [https://www.gegridsolutions.com/products/brochures/powerd\\_vtf/STATCOM\\_GEA31986\\_HR.pdf](https://www.gegridsolutions.com/products/brochures/powerd_vtf/STATCOM_GEA31986_HR.pdf), accessed: 16-Sep-2019.
- [3] Siemens, *Optimal dynamic grid stabilization*, 2019, URL: <https://new.siemens.com/global/en/products/energy/high-voltage/facts/portfolio/svcplus.html>, accessed: 16-Sep-2019.
- [4] K. Sharifabadi, L. Harnefors, H. Nee, S. Norrga, R. Teodorescu, *Design, Control and Application of Modular Multilevel Converters for HVDC Transmission Systems*, John Wiley & Sons, 2016.
- [5] M. Hagiwara, R. Maeda, H. Akagi, “Negative-Sequence Reactive-Power Control by a PWM STATCOM Based on a Modular Multilevel Cascade Converter (MMCC-SDBC)”, *IEEE Trans Ind Appl*, vol. 48, no. 2, pp. 720–729, March 2012.
- [6] O. Oghorada, L. Zhang, “Analysis of star and delta connected modular multilevel cascaded converter-based STATCOM for load unbalanced compensation”, *International Journal of Electrical Power & Energy Systems*, vol. 95, pp. 341–352, February 2018.
- [7] E. Behrouzian, M. Bongiorno, “Investigation of Negative-Sequence Injection Capability of Cascaded H-Bridge Converters in Star and Delta Configuration”, *IEEE Trans Power Electron*, vol. 32, no. 2, pp. 1675–1683, April 2017.
- [8] I. Marzo, J. A. Barrena, A. Sanchez-Ruiz, G. Abad, H. Fernandez-Rebolleda, I. Muguruza, “Reactive power limits of Cascaded H-Bridge STATCOMs in star and delta configuration under negative-sequence current withstanding”, *International Journal of Electrical Power & Energy Systems*, vol. 142, p. 108267, November 2022.
- [9] M. Nieves, J. Maza, J. Mauricio, R. Teodorescu, M. Bongiorno, P. Rodríguez, “Enhanced control strategy for MMC-based STATCOM for unbalanced load compensation”, in *EPE – ECCE Europe*, pp. 1–10, September 2014.
- [10] Y. Yu, G. Konstantinou, C. D. Townsend, R. P. Aguilera, V. G. Agelidis, “Delta-Connected Cascaded H-Bridge Multilevel Converters for Large-Scale Photovoltaic Grid Integration”, *IEEE Trans Ind Electron*, vol. 64, no. 11, pp. 8877–8886, December 2017.
- [11] O. J. K. Oghorada, L. Zhang, “Unbalanced and Reactive Load Compensation Using MMCC-Based STATCOMs With Third-Harmonic Injection”, *IEEE Trans Ind Electron*, vol. 66, no. 4, pp. 2891–2902, June 2019.
- [12] E. R. Rodriguez, R. Leyva, Q. Liu, C. D. Townsend, G. G. Farivar, S. Ceballos, J. Pou, “Enhancing Inductive Operation of Low-Capacitance Cascaded H-Bridge StatComs Using Optimal Third-Harmonic Circulating Current”, *IEEE Trans Power Electron*, p. 10788–10800, March 2021.
- [13] C. Zhao, Z. Wang, Z. Li, P. Wang, Y. Li, “Characteristics Analysis of Capacitor Voltage Ripples and Dimensioning of Full-Bridge MMC With Zero Sequence Voltage Injection”, *IEEE J Emerg Sel Topics Power Electron*, vol. 7, no. 3, pp. 2106–2115, October 2019.
- [14] B. Li, Y. Zhang, G. Wang, W. Sun, D. Xu, W. Wang, “A Modified Modular Multilevel Converter With Reduced Capacitor Voltage Fluctuation”, *IEEE Trans Ind Electron*, vol. 62, no. 10, pp. 6108–6119, April 2015.
- [15] M. Huang, J. Zou, X. Ma, Y. Li, M. Han, “Modified Modular Multilevel Converter to Reduce Submodule Capacitor Voltage Ripples Without Common-Mode Voltage Injected”, *IEEE Trans Ind Electron*, vol. 66, no. 3, pp. 2236–2246, June 2019.
- [16] C. D. Townsend, R. Aguilera, P. Acuna, G. Konstantinou, J. Pou, G. Mirzaeva, G. C. Goodwin, “Capacitance minimization in modular multilevel converters: Using model predictive control to inject optimal circulating currents and zero-sequence voltage”, in *IEEE SPEC*, pp. 1–6, February 2016.
- [17] M. A. Perez, S. Bernet, “Capacitor voltage ripple minimization in modular multilevel converters”, in *IEEE ICIT*, pp. 3022–3027, June 2015.
- [18] K. Li, C. Li, F. C. Lee, M. Mu, Z. Zhao, “Precise control law of MMC and its application in reducing capacitor voltage ripple by injecting circulating current”, in *ICEMS*, pp. 371–377, January 2015.
- [19] T. Tanaka, H. Wang, F. Blaabjerg, “A DC-Link Capacitor Voltage Ripple Reduction Method for a Modular Multilevel Cascade Converter With Single Delta Bridge Cells”, *IEEE Trans Ind Appl*, vol. 55, no. 6, pp. 6115–6126, August 2019.
- [20] D. Mendonça, A. Cupertino, H. Pereira, S. Seleme, R. Teodorescu, “Delta-CHB STATCOM with reduced energy storage requirements based on third harmonic injection”, in *COBEP*, pp. 1–7, January 2021.
- [21] S. K. Chaudhary, A. F. Cupertino, R. Teodorescu, J. R. Svensson, “Benchmarking of Modular Multilevel Converter Topologies for ES-STATCOM Realization”, *Energies*, vol. 13, no. 13, July 2020.
- [22] A. F. Cupertino, J. V. M. Farias, H. A. Pereira, S. I. Seleme, R. Teodorescu, “Comparison of DSCC and SDBC Modular Multilevel Converters for STATCOM Application During Negative Sequence Compensation”, *IEEE Trans Ind Electron*, vol. 66, no. 3, pp. 2302–2312, March 2019.
- [23] D. Mendonça, A. Cupertino, H. Pereira, S. Seleme, R. Teodorescu, “Estratégia de tolerância a falhas para um conversor Delta-CHB STATCOM na região de sobremodulação”, *Revista Eletrônica de Potência*, vol. 25, no. 4, pp. 395–404, December 2020.

- [24] H. A. Pereira, A. F. Cupertino, L. S. Xavier, A. Sangwongwanich, L. Mathe, M. Bongiorno, R. Teodorescu, “Capacitor voltage balance performance comparison of MMC-STATCOM using NLC and PS-PWM strategies during negative sequence current injection”, in *EPE – ECCE Europe*, pp. 1–9, October 2016.
- [25] Q. Tu, Z. Xu, “Power losses evaluation for modular multilevel converter with junction temperature feedback”, in *IEEE PES GM*, pp. 1–7, October 2011.
- [26] *Electronicon, Capacitors for power electronics*, 2023, URL: <https://www.electronicon.com/en/downloads/capacitors-for-power-electronics>, accessed: 07-March-2023.

## BIOGRAPHIES

**Dayane do Carmo Mendonça**, graduated in Electrical Engineering from the Federal University of Viçosa (UFV) in 2019. In April 2021, she was granted a Master’s degree in Electrical Engineering from the Graduate Program in Electrical Engineering at CEFET-MG/UFSJ. She is currently a doctoral student at the Graduate Program in Electrical Engineering at the Federal University of Minas Gerais (UFMG) and a specialist at the Gerência de Especialistas em Sistemas Elétricos de Potência (GESEP-UFV). Her main research interests include modular multilevel converters and renewable energy generation systems.

**João Marcus Soares Callegari**, graduated in Electrical Engineering from the Federal University of Viçosa (UFV) in 2019. In April 2021, he was granted a Master’s degree in Electrical Engineering from the Graduate Program in Electrical Engineering at CEFET-MG/UFSJ. He is currently a doctoral student at the Graduate Program in Electrical Engineering at the Federal University of Minas Gerais (UFMG) and a specialist at the Gerência de Especialistas em Sistemas Elétricos de Potência (GESEP-UFV). His current research and technical interests include design and control of grid-connected multifunctional inverters and reliability of power electronics based systems. Mr. Callegari was the recipient of the President Bernardes Silver Medal in 2019.

**Allan Fagner Cupertino**, (Member, IEEE) was granted the B.S. degree in Electrical Engineering from the Federal University of Viçosa, Viçosa, Brazil, in 2013, the M.S. and Ph.D. degrees in Electrical Engineering from the Federal

University of Minas Gerais, Belo Horizonte, Brazil, in 2015 and 2019, respectively. He was a guest Ph.D. student with the Department of Energy Technology, Aalborg University from 2018 to 2019. Since 2022, he has been with the Electric Engineering Department, Federal Center of Technological Education of Minas Gerais, where he is currently Assistant Professor of Power Electronics. His main research interests include renewable power generation systems, multifunctional inverters, MMC and reliability of power electronics based systems. Dr. Cupertino was the recipient of the President Bernardes Silver Medal in 2013. He is a member of the Brazilian Power Electronics Society (SOBRAEP) and Brazilian Society of Automatics (SBA).

**Heverton Augusto Pereira**, (Member, IEEE) received the B.S. degree from the Federal Federal University of Viçosa (UFV), Viçosa, Brazil, in 2007, the M.Sc. degree from the University of Campinas, Campinas, Brazil, in 2009, and the Ph.D. degree from the Federal University of Minas Gerais, Belo Horizonte, Brazil, in 2015, all of them in Electrical Engineering. He was a visiting Researcher from the Department of Energy Technology, Aalborg University, Denmark, in 2014. He worked as an Adjunct Professor with the Electric Engineering Department, UFV, since 2009. His main research interests include grid-connected converters for PV and wind power systems, and high-voltage dc/flexible ac transmission systems based on MMC.

**Seleme Isaac Seleme Júnior**, holds a degree in Electrical Engineering from the University of São Paulo (1977), a Master’s degree in Electrical Engineering from the Federal University of Santa Catarina (1985) and a PhD in Automatique Productique - Institut National Polytechnique de Grenoble (1994). He took postdocs at the Power Electronics Group at U. C. Berkeley (2002) and at the University of Toulouse, at the LAPLACE Laboratory (2015/16) with a CAPES grant. He is currently a professor at the Federal University of Minas Gerais, with experience in Electrical Engineering and emphasis on Electronic Process Control, Feedback. His activities involve induction motor, electric drives, energy minimization, non-linear control in power electronic converters with application in renewable energy sources and control of electronic ballasts. More recently, as a result of the 2015/16 post-doctorate, he has been working with multilevel converters, coordinating a CAPES-COFECUB cooperation project and supervising doctoral and master’s programs on the subject.